Research Article

Žiga Jelen, Peter Majerič, Matej Zadravec, Ivan Anžel, Martin Rakuša, and Rebeka Rudolf*

Study of gold nanoparticles' preparation through ultrasonic spray pyrolysis and lyophilisation for possible use as markers in LFIA tests

https://doi.org/10.1515/ntrev-2021-0120
received July 28, 2021; accepted November 1, 2021

Abstract: To monitor the progress and prevent the spread of the COVID-19 pandemic in real time and outside laboratories, it is essential to develop effective tests that can ensure rapid, selective, and reliable diagnosis of infected persons in different environments. Key in this regard is the lateral flow immunoassays (LFIAs) that can detect the presence of the SARS-CoV-2 virus quickly, with the aid of nanoparticles (NPs) and specific proteins. We report the use of gold (Au) NPs AuNPs synthesised from a gold(III) chloride tetrahydrate precursor in a USP device and collected in a suspension composed of deionised water with polyvinylpyrrolidone as a stabiliser and cryoprotectant. In combination with freeze-drying of the AuNPs' suspension to achieve water elimination, improved stability, and the target concentration, they exhibit the necessary properties for use as markers in LFIA rapid diagnostic tests. This was confirmed by complementary characterisation determined by using the techniques including inductively coupled plasma-optical emission spectrometry, dynamic light scattering method and zeta-potential, ultraviolet-visible spectroscopy, X-ray diffraction, scanning electron microscopy with energy dispersion spectrometer, and transmission electron microscopy, as well as with the preparation of a prototype LFIA test strip with AuNPs. Thus, such AuNPs, as well as the USP method, show promise for the development of new markers for use in LFIA.

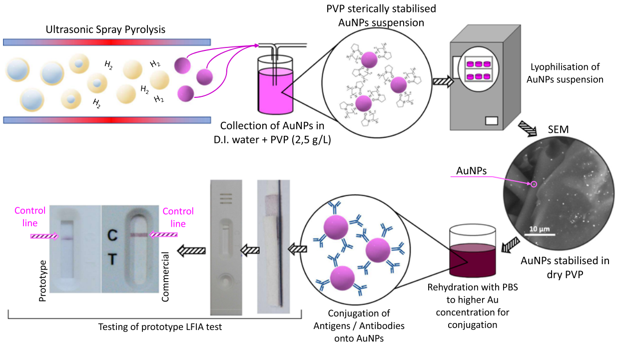

Graphical abstract

Keywords: gold nanoparticles, ultrasonic spray pyrolysis, lyophilisation, LFIA test, COVID-19, conjugation, characterisation

Abbreviations

AuNP	gold nanoparticles
DLS	dynamic light scattering
EDS	energy dispersion spectrometer
FFT	fast Fourier transform
ICP-OES	inductively coupled plasma-optical emission spectrometry
LFIA	lateral flow immunoassay
OD	optical density
PBS	phosphate buffered saline
PEG	polyethylene glycol

*** Corresponding author: Rebeka Rudolf,** Chair of Materials and Forming, University of Maribor, Faculty of Mechanical Engineering, Smetanova Ulica 17, 2000 Maribor, Slovenia; Zlatarna Celje D.O.O., Kersnikova Ulica 19, 3000 Celje, Slovenia, e-mail: rebeka.rudolf@um.si
Žiga Jelen: Chair of Materials and Forming, University of Maribor, Faculty of Mechanical Engineering, Smetanova Ulica 17, 2000 Maribor, Slovenia, e-mail: z.jelen@um.si
Peter Majerič: Chair of Materials and Forming, University of Maribor, Faculty of Mechanical Engineering, Smetanova Ulica 17, 2000 Maribor, Slovenia; Zlatarna Celje D.O.O., Kersnikova Ulica 19, 3000 Celje, Slovenia, e-mail: peter.majeric@um.si
Matej Zadravec: Chair for Power, Process and Environmental Engineering, University of Maribor, Faculty of Mechanical Engineering, Smetanova Ulica 17, 2000 Maribor, Slovenia, e-mail: matej.zadravec@um.si
Ivan Anžel: Chair of Materials and Forming, University of Maribor, Faculty of Mechanical Engineering, Smetanova Ulica 17, 2000 Maribor, Slovenia, e-mail: ivan.anzel@um.si
Martin Rakuša: Department of Neurologic Diseases, Medical Research Department, University Medical Centre Maribor, Ljubljanska Ulica 5, 2000 Maribor, Slovenia, e-mail: ris101@gmail.com

PVP	polyvinylpyrrolidone
SEM	scanning electron microscopy
TEM	transmission electron microscopy
TGA	thermogravimetric analysis
USP	ultrasonic spray pyrolysis
UV-Vis	ultraviolet-visible spectroscopy
XRD	X-ray diffraction

1 Introduction

The entire world is still facing the pandemic of SARS-CoV-2 coronavirus outbreak, which poses one of the deepest threats to global human health and the health system since the end of 2019. Rapid, reliable, and selective diagnosis of the new SARS-CoV-2 coronavirus is extremely important for the identification of infected persons or symptomatic carriers, to prevent or reduce the spread of the virus. Given the severity, speed, and complex mode of COVID-19 transmission, it is particularly important for early diagnosis and understanding of the epidemiological features of this disease to ensure the safety of the population while reducing its transmission. Since the SARS-CoV-2 outbreak, the global health system has been affected severely, mainly due to increased hospitalisation in intensive care units and high mortality rates resulting from severe acute respiratory failure [1,2]. The primary diagnostic methods currently used for diagnosis are based on molecular biology methods (*e.g.* real-time polymerase chain reaction [RT-PCR]), which are ultrasensitive and accurate, but extremely expensive and time-consuming; their implementation also requires expensive and specialised equipment and professionally trained staff [1–5]. Because the COVID-19 pandemic has spread around the world extremely rapidly with millions of cases, these methods alone are not suitable for monitoring the spread and containment of COVID-19 outbreaks in relative real time outside laboratories. The outbreak has also shown that the world is still not adequately prepared for such scenarios, and that there is an urgent requirement to increase research in this field.

Thus, it is essential to develop cheap, fast, reliable, and widely accessible tests that will enable diagnostic detection of COVID-19 in just a few minutes, and the tests themselves must be simple to use in the field. One of the options for prevention is the development of a serologically rapid lateral flow immunoassay (LFIA) test [4]. LFIA tests are simple and portable tests that are often used for both qualitative and quantitative detection of specific antigens and antibodies in a variety of biological samples, including urine, saliva, sweat, serum, plasma, blood, and other fluids, making them useful in many applications, from diagnostics, agriculture, to product quality assessment [6–8].

Pandemic management requires rapid interruption of human-to-human transmission of the virus, rapid identification, early isolation, and care of patients, and accelerated development of diagnostics, therapy, and vaccines [9]. To accelerate the fight against new viruses, the development of nanotechnology, which takes advantage of the many advantages of nanoparticles, can go a long way [10,11]. Metal nanoparticles, among them especially AuNPs, have active optical and electrical properties and a diverse morphology (spheres, cubes, rods, prisms, tetrapods, shells, and hollow structures). AuNPs possess a phenomenon called surface plasmon resonance, which results from the oscillation of free electrons, *i.e.*, plasmons, on their surface, resulting in AuNPs being able to generate a signal (colour change) visible to the naked eye [12–14].

In addition, AuNPs are stable in a variety of media, biocompatible with a variety of physiological fluids, and have a high surface-to-volume ratio, thereby providing special surface chemistry, *i.e.*, bioconjugation of molecules. AuNPs bind easily to viral membrane proteins, and thus, form stable conjugates. Because of all these properties, AuNPs are useful in many applications, including diagnostics, as potential markers in the production of rapid LFIA tests. AuNPs can be prepared by a variety of chemical and physical methods, with each method having certain advantages and disadvantages [15]. For small amounts of AuNPs, most research groups produce the AuNPs themselves, with the most successful methods being Turkevich, Brust-Schriffrin, $NaBH_4$ synthesis, seed growth, vitamin-C synthesis, and various green synthesis methods using different plant extracts to reduce Au^{3+} to Au^0 [16,17]. While these approaches allow some degree of flexibility for researchers, they are not suitable for commercial applications, such as making rapid LFIA tests. In these applications, higher amounts of AuNPs and batch-to-batch consistency play a key role, with the key parameters being size, shape, uniformity, size dispersion, concentration, and application dependent surface modification. Finding accurate data on the methods of companies that produce AuNPs commercially is extremely difficult, but it can be narrowed down to two key existing methods: the first is reduction of Au^{3+} and Au^{1+} solutions, which is a batch process, and enables the preparation of batches up to 350 L and the synthesis of various forms of nanoparticles, such as round, cubic, urchin, or rod shaped [1,2,18,19] and the second is pulsed laser ablation of Au targets, which can be a batch or continuous process, where highly focused laser beams cause ablation of the target material into a gas or liquid. The process allows the production of AuNPs of round and distorted shapes [3–5,20–25].

USP represents a third new method for AuNPs' synthesis, which is a simple and flexible technique where the properties of AuNPs can be controlled easily by changing the USP technological parameters [18–20]. Using the USP method, AuNPs are synthesised from droplets of a metal salt solution (Au-chloride, Au-acetate, and Au-nitrate), generated by ultrasound. These aerosol droplets are then transported with a carrier gas to the reaction furnace, where, after chemical decomposition in the presence of a reduction gas at elevated temperatures, the formation of AuNPs occurs, and finally, they are collected in a suitable collection medium. The collection media typically contain stabilisers, such as Na-citrate, polyvinylpyrrolidone (PVP), or polyethylene glycol (PEG), which prevent further reactions of nanoparticles as they stabilise and prevent AuNPs' agglomeration, even in the freeze-drying process (with the use of a proper stabiliser or cryoprotectant). The process itself allows the production of monodisperse nanoparticles of round and distorted shapes with high capacities [6,26]. The combination of USP and the freeze-drying [27–30] process is novel on the market for AuNPs' preparation, and exhibits an efficient way of AuNP production without the loss of material during drying as well as limiting the exposure of the material to higher temperatures in the drying process, which can cause agglomeration and limit the final AuNPs' functionalities.

The technological advantages and disadvantages of the different AuNPs' synthesis compared to USP are illustrated in Table 1 by showing the target requirements or properties that AuNPs must have. The advantages of the USP process are in the relatively simple setup and operation, a continuous process flow, the possible use of many different precursors (nitrates, chlorides, acetates, inorganic, or organic precursors) [31], with the production of homogeneous chemical compositions and multicomponent particles with the desired stoichiometry [32]. The disadvantages are in the relatively low productivity of the ultrasonic generator as compared to other nebulisers and nozzles, the possibility to obtain aggregated particles, and not being able to use precursor solutions with high concentrations or high viscosity [33,34].

Based on the presented state of the art that AuNPs can be used to produce LFIA tests as markers in these tests, the synthesis of AuNPs has become the main target of research. During the epidemic, LFIA tests proved to be a key factor in controlling the COVID-19 disease, and made it clear that this posed an extraordinary challenge to the nanotechnology profession and its opportunity to finally establish itself on an equal footing with other technologies.

According to a presentation of the current situation in this scientific field, our research work was aimed at confirming the hypothesis that USP could represent the most modern method for the synthesis of AuNPs in suspension, where high productivity of AuNPs with the required final properties would be achieved [35,36]. Therefore, the purpose of this research work was to confirm this hypothesis with USP experimental tests of AuNPs' synthesis, followed by the freeze-drying process, complex conjugation, and prototyping of the LFIA assay. The novel contribution of the present work is in the use of the USP method with stabilisers for the AuNP collection in combination with freeze-drying, for achieving long-term stability of the AuNP markers for use in LFIA tests. This represents a distinct workflow for the production of LFIA tests, utilising the advantages of the processes involved: continuous synthesis, scalability, good nanoparticle size control, and particle stability. To confirm the adequacy of the USP method and the AuNPs' final properties, we used various characterisations. In this way, we wanted to obtain

Table 1: Key technological parameters for AuNPs' synthesis

	Reduction in solutions [13–17,21]	**Pulsed laser ablation** [21,23–25]	**USP** [18,19,22,26]
Size control	Good	Good	Good
Size dispersity	Low	Low	Moderate
Shape control	Spherical, rod, cubic, urchin, shell, *etc.*	Spherical	Spherical
Process type	Batch	Batch or continuous	Continuous
Process repeatability	High batch inconsistencies	Low	Low
Impurities	Possible unreacted contaminants	Low	Possible acidic contaminants
Scalability	Limited to max. 350 L batch size	Highly scalable	Highly scalable
Chemical efficiency	Moderate to high	High	Moderate
Energy intensity	Low	High	Moderate
Drawbacks	Low production rate	Possibility of cross contamination	Explosion risk

baseline results and the adequacy of the hypothesis, so that later we could continue with clinical testing of the LFIA tests based on AuNPs from USP as markers in accordance with European Union legislation.

2 Materials and methods

2.1 Synthesis of AuNPs through USP and the lyophilisation process

A solution of the Au salt precursor (gold chloride [$HAuCl_4 \times 3H_2O$, marked as AuCl], Glentham Life Sciences, Corsham, UK) was prepared by dissolving an appropriate amount of AuCl salt in DI water, while stirring with a magnetic stirrer until the formation of a clear golden-yellow solution. The concentration of [Au] in the chloride precursor solution was 0.5 g/L and the pH was between 3 and 4. The synthesis of AuNPs was performed using the USP method, following a patented method [22]. The synthesised AuNPs were collected in collection bottles in the appropriate collection medium – DI water, in which the stabiliser and cryoprotectant [27,37] polyvinylpyrrolidone (PVP K30, 2.5 g/L, Thermo Fisher Scientific Inc., Schwerte, Germany) were dissolved to stabilise and prevent the agglomeration of AuNPs.

With the aim of using AuNPs as potential markers for rapid LFIA tests, the synthesised AuNPs were pre-dried, as dry AuNPs represent the most optimal form of markers for LFIA test development. Dry AuNPs can be dispersed in a suitable solvent, *i.e.* phosphate buffer saline (PBS), and this step avoids the complex process of solvent removal or replacement during the conjugation process. Preparation of dry AuNPs, *i.e.* drying of the prepared AuNPs' suspension, was performed using the freeze-drying method (lyophilisation). Lyophilisation was chosen since it is a process of removing water from an AuNPs' suspension by sublimation at low temperature, preserving the structure, composition, and stability of the AuNPs. Lyophilisation was performed using a lyophiliser, LIO-2000 FLT (Kambič D.O.O., Semič, Slovenia) [38].

2.2 Preparation of AuNP conjugates

To design a reliable and high-performance rapid LFIA test, it is crucial to appropriately select and use high-quality reagents, which are often not easy to select as there are several viral antigens and/or antibodies to choose from the market. Thus, for the use of AuNPs as potential markers of the LFIA test, it was first necessary to select our target component, *i.e.* a viral antigen. The choice of viral antigen was based on the fact that the viral antigen must be pure, specific, and of high quality [39,40]. From the multitude of antigens on the market, we selected the recombinant antigen SARS-CoV-2 "Spike" protein S1 (aa 1-681) (EMD Millipore Corp., affiliate of Merck KgaA, Darmstadt, Germany). The S1 subunit is exposed to the external environment of the virus and elicits neutralising S1-specific antibody responses easily, *i.e.* antibodies can neutralise the virus by preventing the interaction of S1 with the enzyme ACE-2 [40].

The selected antigen, SARS-CoV-2 "Spike" protein S1, was dissolved in a phosphate buffer before use (PBS, pH = 7.4, Sigma Aldrich Chemie GmbH, Steinheim, Germany). The basis of the conjugation procedure is described in more detail in the literature [3]. Our procedure was done with minor modifications. In general, a suspension of AuNPs (40 nm, 204 ppm) was prepared by dispersing an appropriate amount of dried AuNPs in PBS. To 1 mL of the prepared AuNP suspension, 0.1 mL of self-prepared borate buffer (0.1 M, pH = 8.5) was added with stirring, followed by the addition of 100 µg SARS-CoV-2 antigen dissolved in PBS (1.5 mg/mL). This was followed by 30 min incubation at room temperature ($T = 22°C$). After 30 min, 0.1 mL of BSA dissolved in PBS (10 mg/mL, Acros Organics, Geel, Belgium) was added to the mixture to block the AuNPs' surfaces. After an additional 10 min incubation at room temperature, the prepared mixture was centrifuged at 4°C and 10,000 rpm for 20 min (Centrifuge Rotina 380 R, Andreas Hettich GmbH & Co., Tuttlingen, Germany), to remove any free antigens. The resulting supernatant was removed carefully, and 1 mL of BSA in PBS (1 mg/mL) was added to the resulting pellet conjugate viral antigen-AuNP. This was followed by 5 s stirring in an ultrasonic bath to resuspend the conjugate. The centrifugation and resuspension procedures were repeated twice, with the final addition of 1 mL of PBS. The prepared conjugate viral antigen-AuNP was kept in a refrigerator at 4°C until further use.

Following the same conjugation and purification procedure, 1 mL of conjugate AuNPs-control antibody was also prepared (1.2 mg/mL, Rabbit IgG [Fc specific], Sigma Aldrich Chemie GmbH, Steinheim, Germany). Using the conjugation process, a special ink that contained all the needed components (viral antigen, AuNPs' label, and control antibodies) was prepared, to prepare the conjugate pad of the prototype rapid LFIA test.

2.3 Composition of the prototype LFIA test

The prototype LFIA test strip consisted of four basic components, including a sample pad, a conjugate pad, a nitrocellulose membrane, and an absorbent pad. The choice of substrate for the production of components of the fast LFIA test is influenced by several properties and selection parameters, especially the porosity or volume fraction of the void and/or pores in the paper [41]. Based on this, a 100% cellulose fibre substrate was chosen as the sample and absorbent pads (cellulose fibre sample pads, EMD Millipore Corp., affiliate of Merck KgaA, Darmstadt, Germany); the conjugate pad was made of glass fibres, which provide stability to the conjugates, have a low non-specific binding to the analytes, and allows a constant and uniform flow of the sample, as well as a consistent volume of reagent/buffer (glass fibre diagnostic pad, EMD Millipore Corp., affiliate of Merck KgaA, Darmstadt, Germany) and a nitrocellulose membrane of appropriate thickness (Hi-Flow™ Plus 180, EMD Millipore Corp., affiliate of Merck KgaA, Darmstadt, Germany), were selected as the best compromise between corresponding pore size and slow capillary flow, which ensured adequate time for the reaction between the conjugated AuNPs, the sample, and the test lines.

In the first segment of the experiment, the individual components of the prototype LFIA test strips were pretreated as indicated: the sample and conjugate pads were presoaked in buffer with 3% BSA (w/v) and 1% Tween® 20 (w/v, Sigma Aldrich Chemie GmbH, Steinheim, Germany) for 2 min. The prepared ink (20 or 30 μL of conjugate per cm^2) was applied to the conjugate pad using an automatic

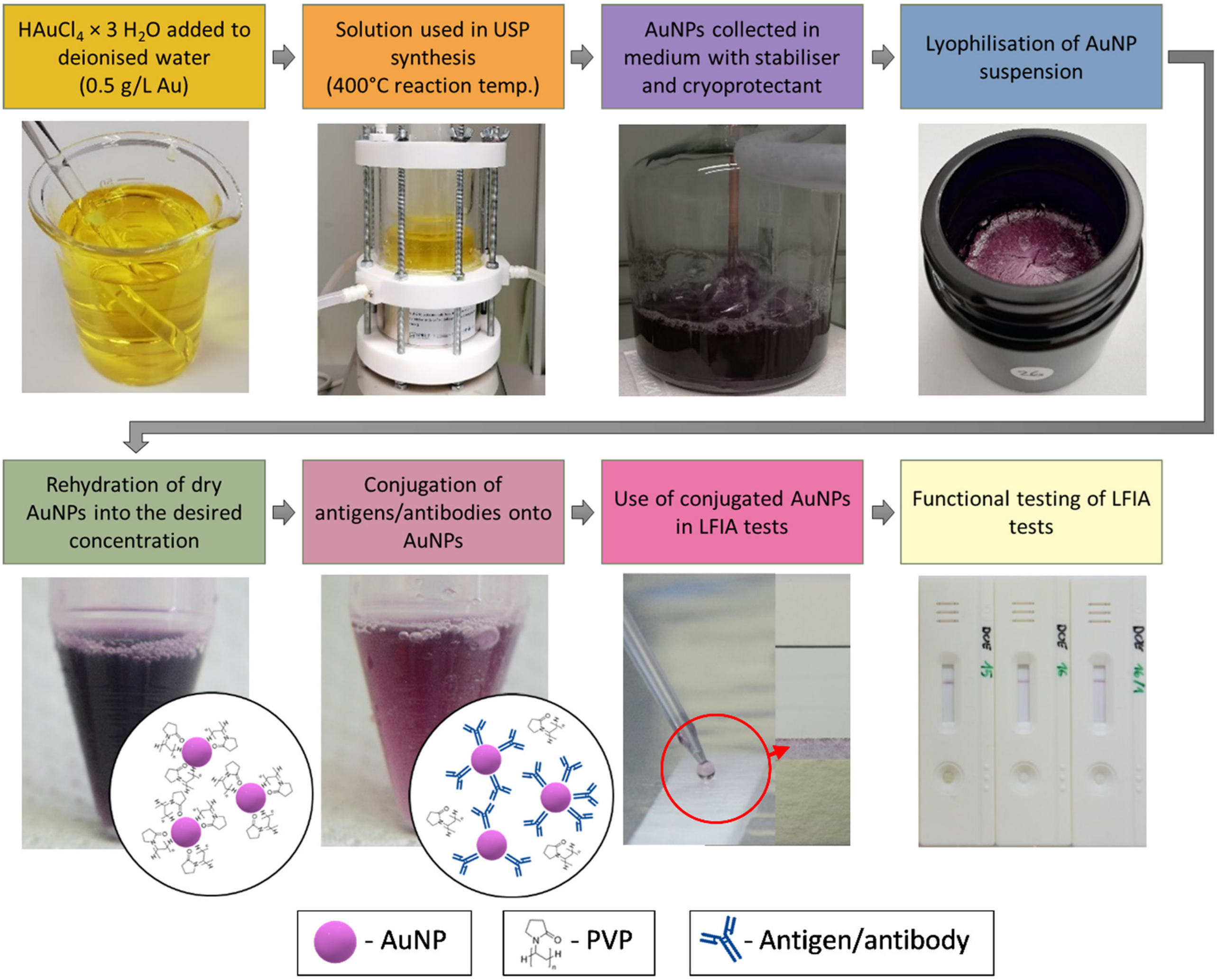

Figure 1: Preparation flow chart of the LFIA tests with key steps from the synthesis of AuNPs with USP, collection of AuNPs and their stabilisation in suspension, lyophilisation of the AuNPs' suspension, rehydration of dry AuNPs into the desired concentration, and conjugation of antigens/antibodies to the final assembly of the prototype LFIA tests with functional testing.

digital pipette (Transferpette® S, Brand GMBH + Co., Wertheim, Germany). A control line (1, 0.5, and 0.2 µg/mL) was applied to the nitrocellulose membrane by hand using a water brush (Koi Water Brush #2, Sakura Colour Products Corp., Osaka, Japan, size: small). The prepared sample pads, conjugate pads, and nitrocellulose membranes were dried at room temperature (T = 22°C) in a desiccator under mild vacuum for 48 h. After 48 h of drying, prototype LFIA test strips were assembled so that all components of the LFIA test strip overlapped each other by 2 mm. Such composition of the prototype LFIA test strip was necessary to ensure the specificity, selectivity, sensitivity, and overall success of the LFIA test, according to the literature [42]. Figure 1 shows the complete preparation of LFIA tests from the phase of AuNPs' synthesis to the production of tests with photographs.

2.4 Characterisation

2.4.1 Thermogravimetric analysis (TGA)

The thermal stability of the $HAuCl_4 \times 3H_2O$ salt was determined by TGA (Mettler Toledo TGA/DSC 3+) and was analysed under the following conditions: inert gas: N_2, gas flow: 50 mL/min, heating rate: 10°C/min, and temperature range: 50–600°C.

2.4.2 Ionic gas chromatography

The real concentration of [Au] in the AuCl precursor (pH = 4) was measured with ion chromatography (IC). Prior to measurements, the sample of the AuCl precursor was diluted tenfold with DI water (resistance 18 MΩ/cm, MilliQ system, Millipore, Bedford, MA, USA). The Dionex ICS 3000 ion chromatograph (Dionex Corporation, Sunnyvale, CA, USA, now under Thermo Fisher Scientific) was used to determine Au and Cl ions under the following experimental conditions: eluent: 23 mm KOH, eluent source: EGC-KOH cartridge II, flow: 1 mL/min, temperature: 30°C, detection: reduced conductivity, damper: Dionex ERS 500, 4 mm; automatic suppression mode, columns: Dionex IonPac AG 18 (4 mm × 50 mm) (precolumn) and Dionex IonPac AS 18 (4 mm × 250 mm), injection volume: 50 µL, and pump flow accuracy: <0.1%.

2.4.3 Inductively coupled plasma-optical emission spectrometry (ICP-OES)

The measurement of the final [Au] concentration in the AuCl aqueous suspension was performed using ICP-OES (Agilent 720/725 ICP-OES, Agilent Technologies, Santa Clara, USA). Prior to analysis, the sample was acidified with aqua regia, and the analysis was performed at the following operating parameters: RF power: 1.5 kW, nebuliser: Meinhard, plasma flow: 15 L/min, nebuliser flow gas: 0.85 L/min, make up gas flow: 0.28 L/min, and reaction gas flow: 4.0 mL/min. Calibration of the instrument was performed with matrix standard calibration solutions. The relative measurement uncertainty was estimated to be ±3%.

2.4.4 X-ray diffraction (XRD) measurements

Additional XRD measurements of dry and unconjugated AuNPs were performed with a Panalytical XPERT Pro PW 3040/60 goniometer 2theta 10–90° with a step of 0.002° and a time of 100 ms per step. The anode was Cu (Kalfa = 0.154 nm) with a current of 40 mA and a voltage of 45 kV.

2.4.5 Dynamic light scattering (DLS) method and zeta (ζ) potential measurements

DLS measurements of the hydrodynamic size distribution of AuNPs in aqueous suspension and measurements of ζ potential were performed with the Malvern Zetasizer Nano ZS instrument (Malvern Panalytical, Worcestershire, UK). The hydrodynamic size distribution of AuNPs was measured using disposable plastic cuvettes and ζ potential measurements were done using a closed capillary cell with electrodes. DLS and ζ potential measurements were performed with the following parameters for AuNP material: refractive index (RI) = 0.2, absorption = 3.32; the suspension properties were: dispersant = water, RI = 1.33, viscosity = 0.887 cP, temperature = 25°C, equilibration time = 30 s, angle of incidence = 173° backscatter, and dielectric constant = 78.5. Measurements were performed in 10 series, 10 s per series, and the measurements were repeated 3 times.

2.4.6 Ultraviolet-visible (UV-Vis) spectroscopy

UV-Vis absorption spectroscopy was used to characterise the optical and structural properties of the aqueous suspension of AuNPs in the ultraviolet and visible light spectra. Measurements of the absorbance spectrum of the prepared aqueous suspension of AuNPs were measured using a UV-VIS spectrophotometer, Tecan Infinite M200 (Tecan Group Ltd, Männedorf, Switzerland), using a special microplate, with the following parameters:

sample volume: 300 µL, absorbance range: λ = 400 and 800 nm, and no. of flashes: 5×.

2.4.7 Scanning electron microscopy (SEM) with energy dispersion spectrometer (EDS)

SEM (FEI Sirion 400 NC, FEI Technologies Inc., Hillsboro, Oregon, USA) was used to characterise the shape, size, and morphology of the AuNPs in dried form from an aqueous suspension and pads coated with conjugated AuNPs. A semiqualitative and semiquantitative microchemical analysis of the suspension was done with an EDS (EDS INCA 350, Oxford Instruments, Abingdon, UK). A drop of AuNPs' suspension, stabilised with PVP, was pipetted onto a graphite tape. The tape was air-dried at room temperature (T = 22°C) for SEM-EDS investigations. The analysis was performed under the initial parameters: high vacuum (HV): 10 kV, back scatter detector and magnification: 100–5,000×.

2.4.8 Transmission electron microscopy (TEM)

JEOL 2100 (JEOL, Japan) and JEOL JEM-2200FS HR (JEOL, Japan) equipment operating at 200 kV were used for the TEM investigation. A drop of PVP-stabilised AuNPs' suspension was put on a copper TEM grid with an amorphous carbon film. The grids were then dried before they were used for the TEM investigations.

2.4.9 Statistics

ImageJ software was used for the size measurements of AuNPs from the SEM micrographs. A total of 400 AuNPs were measured from 20 SEM images. Bin sizes of 14 nm were used for the size distribution representations. Mean values were calculated from the measured particle sizes. The mean values and standard deviations for the DLS size measurements with distributions and ζ potential measurements of AuNPs were given by the Malvern Zetasizer measurement software.

3 Results

3.1 AuCl precursor

3.1.1 TGA analysis

According to the literature [26], complete thermal decomposition of metal chlorides such as HAuCl4 × 3H$_2$O usually occurs in three stages, with gradual decomposition of the salt. The TGA-DT curve (Figure 2) revealed that the first stage of thermal decomposition of $HAuCl_4 \cdot 3H_2O$ began immediately after melting, at 73°C, and continued until approx. 178°C, with 13.9% weight loss. The main decomposition processes are the processes of dehydration and

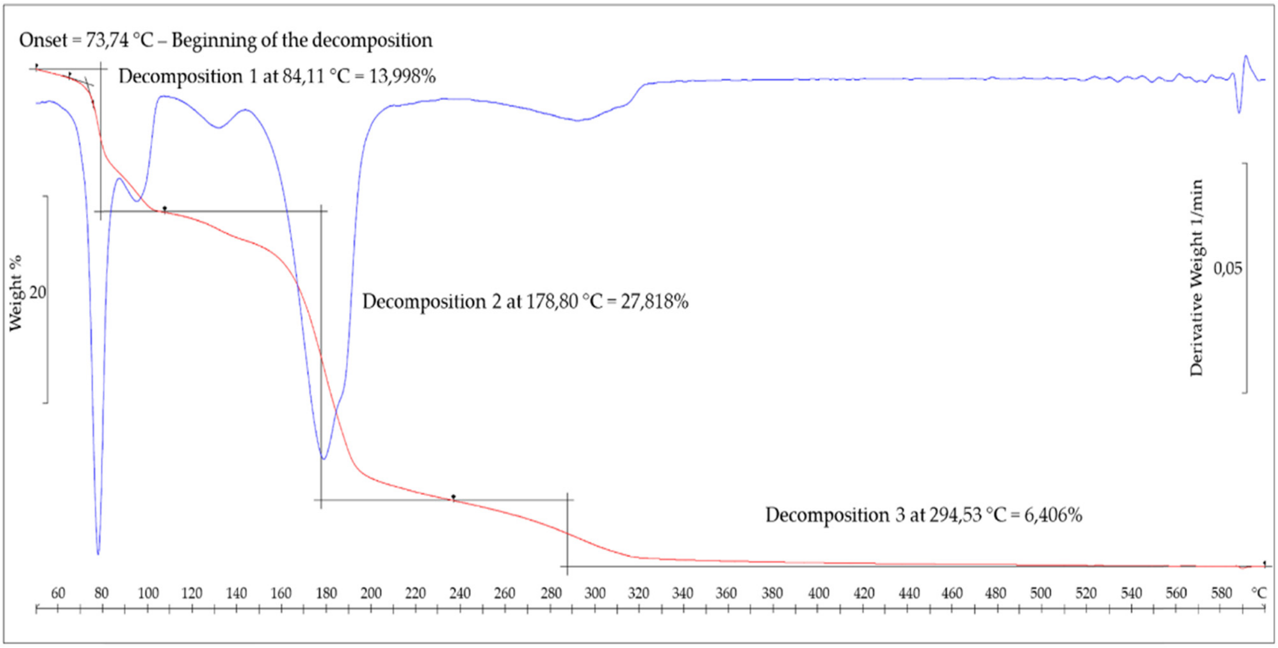

Figure 2: TGA-DT curve for gold chloride ($HAuCl_4 \times 3\ H_2O$), 10°C/min, in nitrogen.

dechlorination, which take place simultaneously, and the thermal decomposition of the first stage can be expressed by equation (1):

$$HAuCl_4 \times 3H_2O \rightarrow AuCl_3 + HCl + 3H_2O. \quad (1)$$

The second stage of thermal decomposition took place in the temperature range between 178 and 294°C, with 27.8% mass loss, and the thermal decomposition of the second phase can be expressed by equation (2):

$$AuCl_3 \rightarrow AuCl + Cl_2. \quad (2)$$

The third stage of thermal decomposition took place in the temperature range between 294 and 320°C, with 6.4% weight loss. The final product of the third stage thermal decomposition is the formation of pure Au. Equation (3) represents the thermal decomposition of the third stage:

$$2AuCl \rightarrow 2Au + Cl_2. \quad (3)$$

The total loss of mass in conversion of $HAuCl_4 \times 3H_2O$ salt to pure Au was 51.7%.

3.1.2 Ionic gas chromatography

Based on the results of IC, we can see that the AuCl precursor solution [500 ppm] contained as much as 570 ppm Au and 281 ppm Cl^-. The excess Au concentration was most likely due to errors in the weighing of the Au salt during the preparation of the precursor, or inaccurate dilution of the precursor solution with DI water.

3.2 PVP-stabilised AuNPs' suspension

3.2.1 ICP-OES analysis

The concentration of Au in the final AuNPs' suspension was 64 ppm. Higher concentrations of AuNPs (with values above 1,000 ppm) were achieved by redissolving the freeze-dried AuNPs in smaller volumes of solvent. For our own conjugation experiments we prepared a suspension with a measured Au concentration of 204 ppm.

3.2.2 XRD analysis

XRD analysis of dry and unconjugated AuNPs showed standard Bragg reflections (111), (200), (220), (311), and (222), corresponding to a face centred cubic lattice for Au. Characteristic dots (Figure 3) have been compared with literature data on structural factors [43]. The higher intensities at peaks (111) and (200) signify preferential growth of Au in these directions.

3.2.3 DLS analysis and ζ potential measurements

DLS analysis can reveal several key AuNPs' characteristics quickly, such as shape, hydrodynamic size distribution, hydrodynamic radius, and state of the AuNPs' agglomeration, by monitoring the Rayleigh scattering of a laser beam, caused by the Brownian motion of AuNPs smaller than the incident light wavelength at a fixed scattering angle [19]. The DLS analysis of PVP-stabilised AuNPs' suspension revealed three different groups of AuNPs with different size distributions (in intensity%): Group 1 contained 3.6% AuNPs with diameters between 10 and 200 nm, Group 2 contained 94.3% AuNPs with diameters between 200 and 800 nm, while Group 3 contained 2.1% AuNPs with diameters > 4000 nm. The average AuNPs' size (together with their standard deviation) was 418.3 ± 18 nm.

The ζ potential of the AuNPs' surface with standard deviation was −3.22 ± 4.13 mV. This value indicates the stability of the AuNPs and their ability to resist agglomeration and coalescence.

AuNPs conjugated with SARS and Rabbit IgG were both prepared from an AuNPs' suspension with an Au concentration of 204 ppm. The hydrodynamic radius of the AuNPs decreased after conjugation and the subsequent washing with PBS. This resulted in an average size distribution of 114.2 ± 0.75 nm for conjugate viral antigen-AuNPs, and an average size distribution of 82.64 ± 2.51 nm for conjugate Rabbit IgG-AuNPs.

3.2.4 UV-Vis spectroscopy

UV-Vis spectroscopy is a reliable technique for determining the absorption band and level of aggregation of

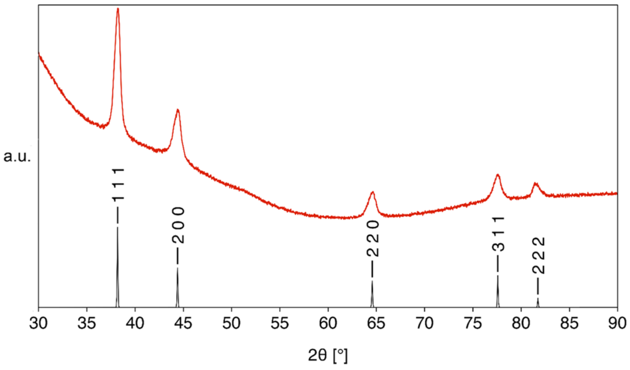

Figure 3: XRD spectrum of unconjugated freeze-dried AuNPs, within a PVP matrix.

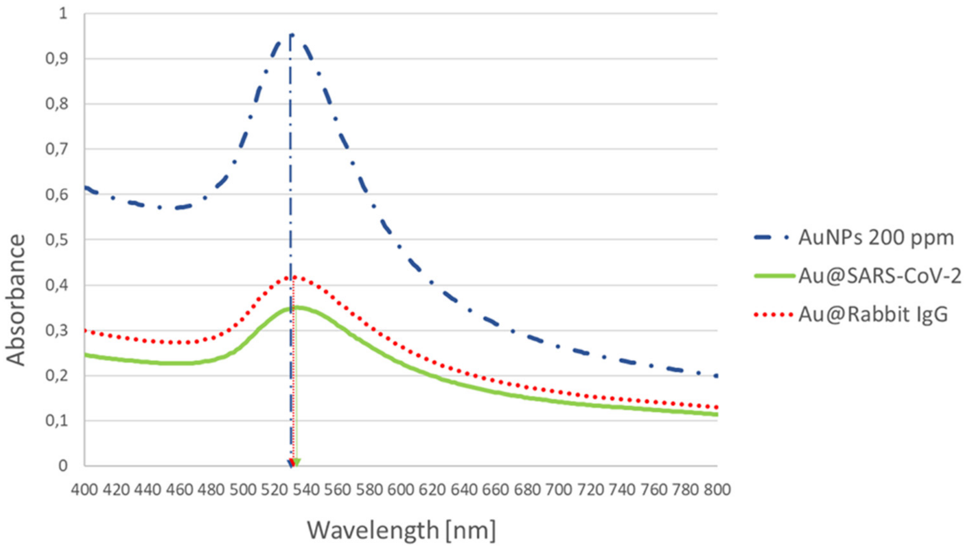

Figure 4: UV-Vis spectrum of: Unconjugated AuNPs (200 ppm), Au@SARS-CoV-2: AuNPs conjugated with SARS-CoV-2 antigens, and Au@Rabbit IgG: AuNPs conjugated with Rabbit IgG antibodies.

synthesised AuNPs. The maximum absorbance for surface plasmon resonance occurred at approximately $\lambda_{\max}$ = 530 nm, which indicates the stable state of the AuNPs clearly (Figure 4). The colour of the AuNPs' suspension was dark purple. The narrow band of the curve corresponds mostly to the monodisperse nature of AuNPs, without any aggregation and agglomeration. The characteristic peak shift to higher wavelengths is indicative of the successful conjugation of USP AuNPs with viral antigen and Rabbit IgG [44].

3.2.5 SEM and TEM investigations

PVP-stabilised AuNPs in the suspension were characterised with SEM and TEM techniques in order to observe the real size and shape of the nanoparticles. From Figure 5 it can be seen that the AuNPs were mostly spherical shaped (not 100%). Additionally, manually performed size analysis on 20 SEM micrographs (400 AuNPs) revealed that about 70% of the AuNPs were in the size range of 40–80 nm. AuNPs had an average diameter of 60 ± 20 nm. This was determined based on the measurement of the AuNPs' diameters. More detailed results of AuNPs' size distribution are shown in Figure 6.

Several AuNPs were analysed at atomic resolution to confirm their crystal structure. Gold has a cubic crystal structure (Fm-3m, No. 225). The distances of the atomic planes were measured on the investigated AuNPs, and the Miller indices (*h k l*) were determined using the fast Fourier transform (FFT) mathematical method. Figure 7 shows an example of an investigated AuNP with identified Miller indices and measured distances between atomic planes. The AuNP is about 9 nm in diameter, and has a distance of 0.242 nm between its atomic planes in the

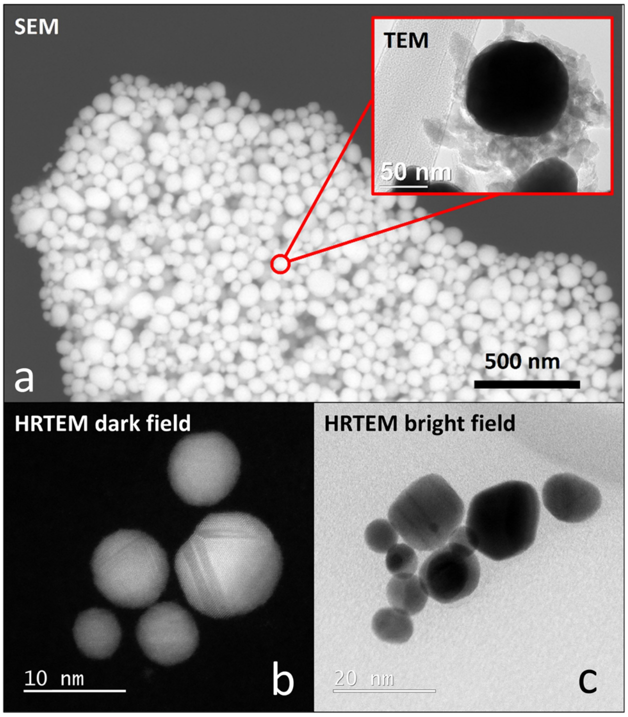

Figure 5: (a) SEM micrograph of PVP-stabilised AuNPs with a TEM of representative AuNP, HRTEM image of the AuNPs: (b) dark and (c) bright fields showing their morphology, structures, some dislocations, and twinning.

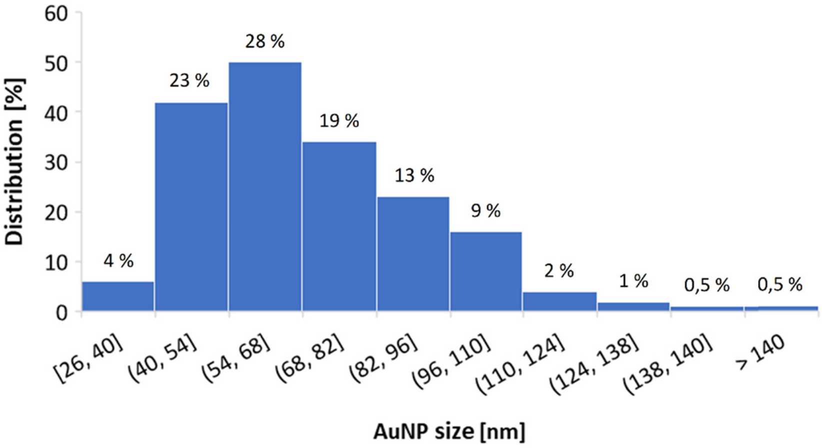

Figure 6: Size distribution of AuNPs, obtained from 20 SEM images (400 AuNPs analysed).

given orientation. This distance corresponds to a reference diffraction card for the Fm-3m crystal structure, which has an atomic plane distance of 0.239 nm for the Miller index *h k l* 1 1 1.

3.2.6 LFIA – SEM-EDS analysis of conjugate pads

Conjugate pads from a commercially available SARS-CoV-2 LFIA (Nova test – one step diagnostic rapid test [cassette]; SARS-CoV-2 antigen rapid test kit; LOT:20201105) test and our own prototype LFIA tests were compared by visual comparison and SEM-EDS analysis, and are shown in Figure 8.

Visual comparison shows clearly a drastic difference in the colour intensity of the conjugate pad, indicating a much higher loading of AuNPs on the commercial test (Figure 8a and b).

SEM images show that the AuNPs on the commercial test are clumped together on the edges of the glass fibres (Figure 8c), while our own test shows much more monodispersed AuNPs (Figure 8d). This is indicative of the standard procedure of drying the sprayed AuNPs on the conjugate at 37°C [2–5], while we dried ours in an

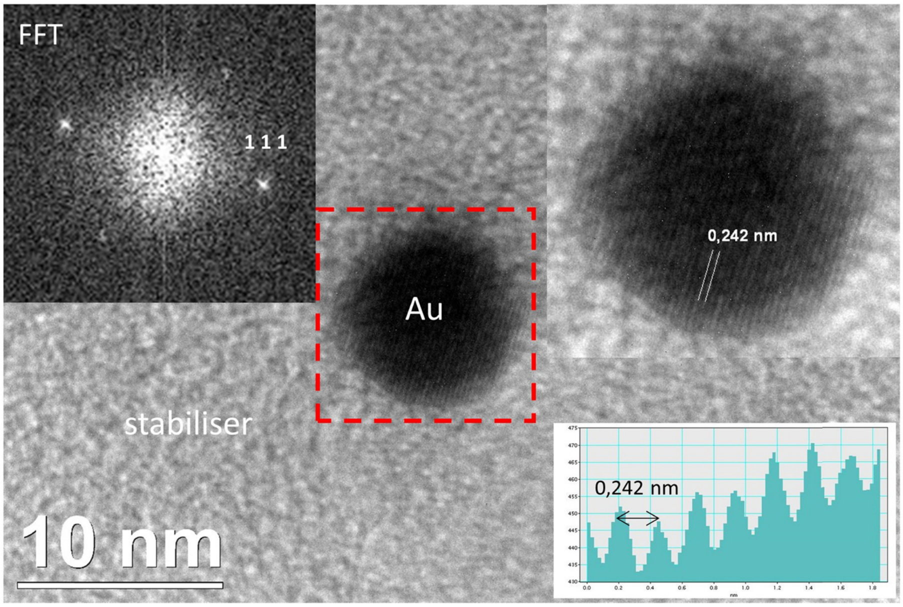

Figure 7: HRTEM image of an AuNP with FFT simulation taken from the area of the red dashed square around the AuNP, the AuNP with visible atomic planes 0.242 nm, and the corresponding profile across the atomic planes.

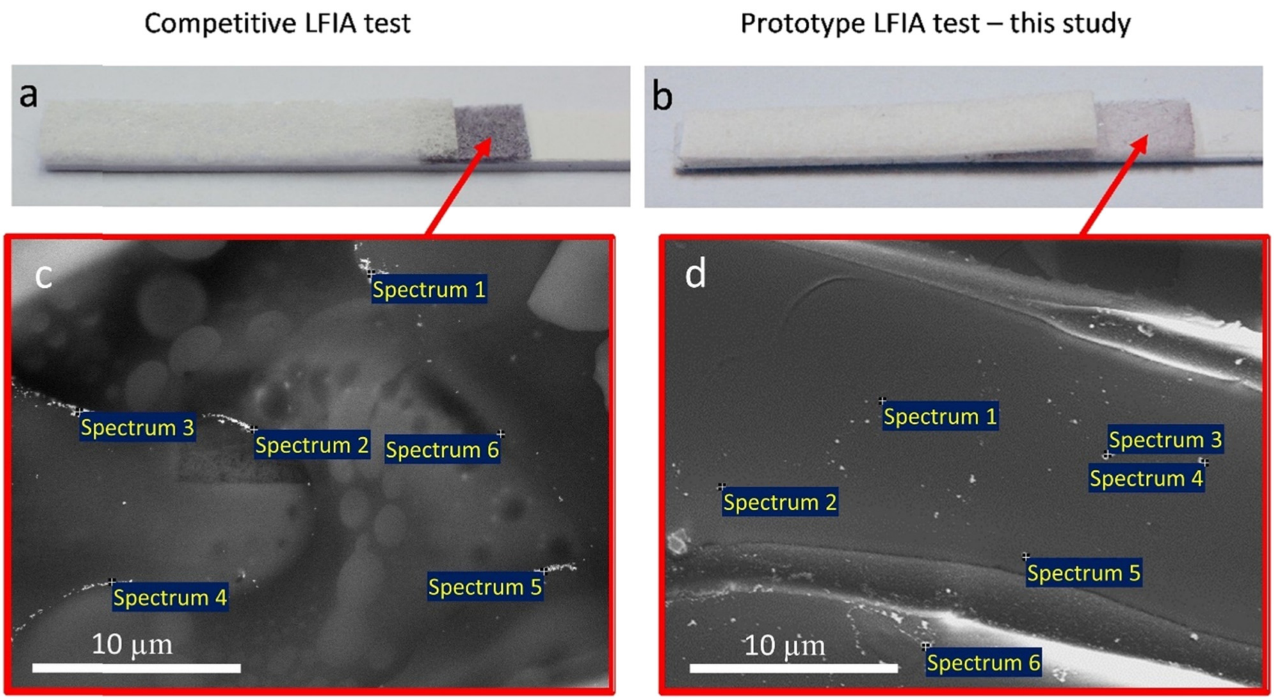

	C	O	Na	Al	Si	Ca	Au
Spectrum 1	59.35	28.44	0.67	1.52	4.76	3.26	2.00
Spectrum 2	65.26	19.52	1.43	1.72	6.84	4.93	0.30
Spectrum 3	59.66	22.95	1.55	1.65	6.05	4.66	3.47
Spectrum 4	61.21	19.57	1.60	1.65	4.61	3.03	8.34
Spectrum 5	54.88	22.80	0.81	2.13	9.08	5.61	4.70
Spectrum 6	43.43	34.95	1.03	3.09	11.06	5.37	1.06
Mean	57.30	24.71	1.18	1.96	7.07	4.48	3.31
Std. deviation	7.57	5.98	0.40	0.59	2.55	1.09	2.94

	C	O	Na	Al	Si	Ca	Au
Spectrum 1	21.71	52.53	3.32	3.48	14.53	4.34	0.09
Spectrum 2	27.89	44.51	25.36	0.18	0.59	0.86	0.62
Spectrum 3	10.15	17.09	1.47	0.50	18.85	44.97	6.98
Spectrum 4	18.36	15.36	2.13	2.82	20.89	35.53	4.91
Spectrum 5	23.28	17.32	2.04	5.23	29.74	19.69	2.69
Spectrum 6	14.34	22.79	2.73	4.87	21.50	31.35	2.41
Mean	19.29	28.27	6.18	2.85	17.68	22.79	2.95
Std. deviation	6.40	16.09	9.42	2.14	9.74	17.65	2.61

Figure 8: Comparison: macro-view: (a) commercially available LFIA test and (b) prototype LFIA test-this study; SEM micrograph with corresponding EDS spectra on selected sites: (c) conjugate pad of the commercially available LFIA test and (d) conjugate pad of the prototype LFIA test-this study.

exicator under a mild vacuum, achieving a higher drying rate, thus limiting the time for agglomeration.

SEM-EDS analysis confirmed the presence of AuNPs with the characteristic EDS spectra for Au, detected on the bright spots (AuNPs) that are visible on Figure 8a and b. The detection of C and O corresponds to the presence of organic components, while the presence of O, Na, Al, Si, and Ca corresponds to the expected spectrum of the glass fibres.

The functionality of the prototype LFIA tests based on AuNPs was confirmed by observing the colouring of the control line, which was light pink in colour, as presented in Figure 9a, compared to the control line on a commercial test. It is visible that the control line in our test is lighter in colour, which indicates indirectly that there was no 100% release of AuNPs from the conjugate pad.

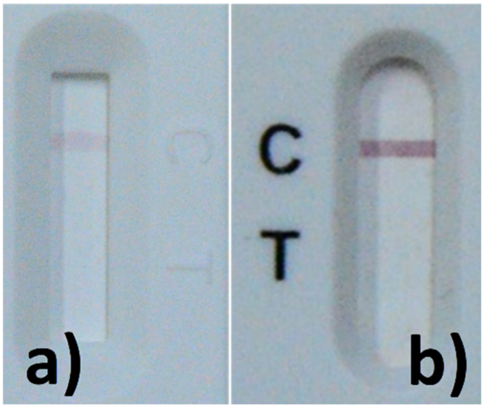

Figure 9: (a) Control line on the prototype LFIA strip and (b) control line on the commercial LFIA strip.

4 Discussion

4.1 Production of AuNPs

AuNPs were synthesised using the USP method under optimised parameters from a gold(III) chloride tetrahydrate precursor, with an Au concentration of 570 ppm in the precursor. The heating and flow parameters in the USP were chosen with regard to previous works [20,45,46], and based on the results of TGA analysis (130°C [evaporation zone], 400°C [reaction zone], and 400°C [sintering zone], with a gas flow of 6 L/min of both N_2 and H_2).

4.2 Conjugation of AuNPs

To achieve a higher concentration and stability of AuNPs and a higher Optical Density (OD), the initial suspension was freeze-dried with an Au concentration of 64 ppm and 0.26 OD. In the next step, the dry AuNP + PVP cake was redissolved in PBS to achieve a final Au concentration of 204 ppm (confirmed with ICP-OES) and OD of 0.91. The actual shape of AuNPs was obtained using SEM (Figure 5), which was used to determine the actual size and size distribution (Figure 6).

Commercially available Au nanospheres used for the LFIA are available from several vendors, and are offered in a variety of sizes (2–240 nm), with a variety of surface modifications (Bare-Citrate, aminated, carboxyl, PEG, PVP, tannic acid, streptavidin, polystyrene, and silica shelled), and at different concentrations, most often marked as OD, which is, for AuNPs, determined at a wavelength of 520 nm. AuNPs are available from 1 OD to 20 OD (BBI Solutions, The BBI Group and nanoComposix). The OD and visibility of the test lines have a direct correlation with the visual readability of LFIA tests, and, as such, a higher OD is beneficial [47,48].

The prepared 0.91 OD suspension in this study was conjugated with SARS-CoV-2 viral antigen and control Rabbit IgG. Successful conjugation was confirmed with UV-Vis (Figure 4).

The hypothesised binding mechanics of AuNPs with S1 (aa1-681) [49,50] and Rabbit IgG are *via* the S1's and IgG C-terminals' binding to the surface of the AuNPs, respectively. The C-terminus is the carboxyl group terminated end of a protein (as opposed to the N-terminal). The addition of borate buffer with a high pH of 8.5 "activates" the C-terminus by creating a sodium carboxylate anion, which can bind directly to the surface of AuNPs with a similar mechanism as sodium citrate [51], by substituting the PVP. Consequently, the DLS measurement fell drastically after conjugation to 114.2 ± 0.75 nm for conjugate viral antigen-AuNPs, and an average hydrodynamic size distribution of 82.64 ± 2.51 nm for conjugate Rabbit IgG-AuNPs. This is a result of the washing steps during conjugation that removed the excess of substituted PVP.

OD values can provide us with an idea of protein binding, which, with USP AuNPs after conjugation with SARS-CoV-2, fell to 0.33 from 0.91, and with Rabbit IgG fell to 0.62 from 0.91. This indicates that USP AuNPs with an average size of 60 ± 20 nm have a much higher protein binding with Rabbit IgG antibodies than with SARS-CoV-2 antigens [40]. The significant drop in OD was due to the loss of AuNPs during the washing steps, which was visible with the naked eye, as presented in Figure 10. The combination of DLS size difference and the difference in OD between SARS-CoV-2 antigens and Rabbit IgG antibodies suggests that better binding and, consequently, less loss in OD can be achieved with size optimisation of AuNPs for specific proteins.

4.3 LFIA test

The conjugated suspensions were applied to conjugation pads as described in Section 2.3. Initially, the USP AuNPs showed a higher affinity for the nitrocellulose membrane, in that they failed to flow the entire length of the test strip. As an increase in Tween 20 and BSA concentration on the sample pad seemingly had no effect, we also opted to pretreat the conjugation pad with the same procedure as of the sample pad (described in Section 2.3) before applying the conjugated AuNPs. This ensured a reliable release of AuNPs, and ensured a continuous flow over the whole nitrocellulose membrane, as presented in Figure 9. In order to get a better understanding of the difference between our own LFIA test strip and a commercially available test strip for SARS-CoV-2, we focused mainly on the conjugation pad, which we imaged with SEM

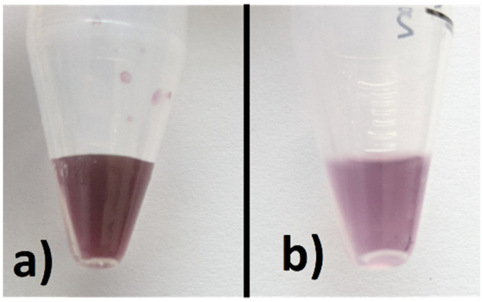

Figure 10: (a) Unconjugated AuNPs, and (b) AuNPs conjugated with SARS-CoV-2 and washed.

and used EDS to confirm the presence of Au. The results are presented in Figure 8, where we noticed that the AuNPs in the commercial test were clumped together on the edges of the glass fibres that compose the conjugation pad, while the AuNPs on the prototype test in this study were much better dispersed. A key difference that is visible to the naked eye is the stark contrast in colour intensity between our test and the commercial test, which was much darker. Therefore, while we were able to confirm the functionality of our test, (as shown in Figure 9a) with the appearance of the control line, it was much less visible when compared to the commercial test. We can attribute this to the much lower OD of our conjugate and the lower loading of AuNPs' on the conjugate pad. This signifies a need for us to increase the OD density of our AuNPs suspensions considerably, and an added potential to reduce the loss of conjugate and AuNPs during conjugation by optimising the size of the AuNPs. Besides offering a considerable increase in productivity, the relatively simple operation and repeatability of USP allow for the production of product lines with different AuNPs' sizes and concentrations by simply changing the initial concentration of Au^{3+} in the precursor solution.

4.4 Future clinical testing

One of the limitation of our LFIA tests is that they were not yet tested in the clinical environment. Thus, we may not report on the test's sensitivity, limit of detection, reproducibility, and re-usability, as well as the commercialisation aspects. However, recently, we have begun a clinical trial, which was approved by the Slovenian National Medical Ethics Committee (0120-92/2021/3, 18.03.2020) and the Agency for Medicinal Products and Medical Devices of the Republic of Slovenia (341-1/2021-10, 30.07.2021). In the clinical trial, we will compare the detection of the corona virus in the mucosae or blood serum using our tests with the PCR test results, and report our results in future publications.

5 Conclusion

The following conclusions can be drawn from the current research study:

1. USP synthesis can produce AuNPs in suspension with suitable size, shape, and monodispersity, which allowed AuNPs to be freeze-dried without changing their properties, and thus, the possibility of using them without further preparation as markers in LFIA tests.
2. Conjugation of AuNPs with SARS-CoV-2 in suspension caused a decrease in OD from 0.91 to 0.33, and in the case of Rabbit IgG from 0.91 to 0.62. This indicates that AuNPs with an average size of 60 ± 20 nm have a much higher protein binding with Rabbit IgG antibodies than with SARS-CoV-2 antigens.
3. The prepared AuNPs' suspension was conjugated successfully with SARS-CoV-2 viral antigen and control Rabbit IgG antibodies, which was confirmed by UV-Vis measurement.
4. Treatment of the conjugation pad according to a similar procedure as the sample pads allows reliable release of AuNPs, and thus, ensures their continuous flow across the entire nitrocellulose membrane, which means that the LFIA test will work.
5. The key requirement for the preparation of an appropriate LFIA test is a high enough OD of AuNPs' suspensions, which must remain as high as possible during the conjugation process and the production of LFIA tests.

Acknowledgements: The authors acknowledge Dr Darja Feizpour from the Department of Physics and Chemistry of Materials at the Institute of Metals and Technology (IMT) Ljubljana, Slovenia, for performing the TEM investigations for the research under an order from Zlatarna Celje D.O.O. Slovenia. The authors also thank Ms. Doris Golub for her help in conducting the research.

Funding information: This research was funded by the Slovenian Research Agency, Grant number ARRS-Rpprog-JP-COVID-19-077 and Training and funding of a Young Researcher, (Co) financing agreement nos. 1000-19-0552, 1000-20-0552, and 1000-21-0552.

Author contributions: All authors have accepted responsibility for the entire content of this manuscript and approved its submission.

Conflict of interest: The authors declare no conflict of interest.

Data availability statement: The datasets generated during and/or analysed during the current study are available from the corresponding author on reasonable request.

References

[1] Moitra P, Alafeef M, Dighe K, Frieman MB, Pan D. Selective naked-eye detection of SARS-CoV-2 Mediated by N gene targeted antisense oligonucleotide-capped plasmonic nanoparticles. ACS Nano. 2020;14(6):7617–27.

[2] Wen T, Huang C, Shi FJ, Zeng XY, Lu T, Ding SN, et al. Development of a lateral flow immunoassay strip for rapid detection of IgG antibody against SARS-CoV-2 virus. Analyst. 2020;145(15):5345–52.

[3] Li Z, Yi Y, Luo X, Xiong N, Liu Y, Li S, et al. Development and clinical application of a rapid IgM-IgG combined antibody test for SARS-CoV-2 infection diagnosis. J Med Virol. 2020;92(9):1518–24.

[4] Nuccetelli M, Pieri M, Gisone F, Bernardini S. Combined anti-SARS-CoV-2 IgA, IgG, and IgM detection as a better strategy to prevent second infection spreading waves. Immunol Invest. 2020;1–13.

[5] Huang C, Wen T, Shi FJ, Zeng XY, Jiao YJ. Rapid detection of IgM antibodies against the SARS-CoV-2 virus *via* colloidal gold nanoparticle-based lateral-flow assay. ACS Omega. 2020;5(21):12550–6.

[6] Koczula KM, Gallotta A. Lateral flow assays. Essays Biochem. 2016;60(1):111–20.

[7] Bahadır EB, Sezgintürk MK. Lateral flow assays: principles, designs and labels. TrAC - Trends Anal Chem. 2016;82:286–306. doi: 10.1016/j.trac.2016.06.006

[8] Grant BD, Anderson CE, Williford JR, Alonzo LF, Glukhova VA, Boyle DS, et al. SARS-CoV-2 coronavirus nucleocapsid antigen-detecting half-strip lateral flow assay toward the development of point of care tests using commercially available reagents. Anal Chem. 2020;92(16):11305–9.

[9] Sellner J, Jenkins TM, Oertzen TJ, Bassetti CL, Beghi E, Bereczki D, et al. A plea for equitable global access to COVID-19 diagnostics, vaccination and therapy: the NeuroCOVID-19 task force of the European academy of neurology. Eur J Neurol. 2021;28:3849–55.

[10] Rabiee N, Bagherzadeh M, Ghasemi A, Zare H, Ahmadi S, Fatahi Y. et al. Point-of-use rapid detection of SARS-CoV-2: nanotechnology-enabled solutions for the COVID-19 pandemic. Int J Mol Sci. 2020;21:1–23.

[11] Gupta R, Sagar P, Priyadarshi N, Kaul S, Sandhir R, Rishi V, et al. Nanotechnology-based approaches for the detection of SARS-CoV-2. Front Nanotechnol. 2020;2:1–14.

[12] Penders J, Stolzoff M, Hickey DJ, Andersson M, Webster TJ. Shape-dependent antibacterial effects of non-cytotoxic gold nanoparticles. Int J Nanomed. 2017;12:2457–68.

[13] Amendola V, Pilot R, Frasconi M, Maragò OM, Iatì MA. Surface plasmon resonance in gold nanoparticles: a review. J Phys Condens Matter. 2017;29(20):203002.

[14] Adekoya JA, Ogunniran KO, Siyanbola TO, Dare EO, Revaprasadu N. Band structure, morphology, functionality, and size-dependent properties of metal nanoparticles. In: Seehra MS, Bristow AD, editors. Noble and precious metals - properties, nanoscale effects and applications. IntechOpen; 2018. p. 15–42.

[15] Herizchi R, Abbasi E, Milani M, Akbarzadeh A. Current methods for synthesis of gold nanoparticles. Artif cells, Nanomed Biotechnol. 2016;44(2):596–602.

[16] Sengani M, Grumezescu AM, Rajeswari VD. Recent trends and methodologies in gold nanoparticle synthesis – A prospective review on drug delivery aspect. OpenNano. 2017;2(January):37–46. doi: 10.1016/j.onano.2017.07.001.

[17] Daruich De Souza C, Ribeiro Nogueira B, Rostelato MECM. Review of the methodologies used in the synthesis of gold nanoparticles by chemical reduction. J Alloy Compd. 2019;798:714–40. doi: 10.1016/j.jallcom.2019.05.153.

[18] Rudolf R, Shariq M, Veselinović V, Adamović T, Bobovnik R, Kargl R, et al. Synthesis of gold nanoparticles through USP. Contemp Mater. 2018;9(1):106–12.

[19] Golub D, Ivanič A, Majerič P, Tiyyagura HR, Anžel I, Rudolf R. Synthesis of colloidal Au nanoparticles through ultrasonic spray pyrolysis and their use in the preparation of polyacrylate-AuNPs' composites. Materials (Basel). 2019;12(22):1–17.

[20] Rudolf R, Majerič P, Tomić S, Shariq M, Ferčec U, Budič B, et al. Morphology, aggregation properties, cytocompatibility, and anti-inflammatory potential of citrate-stabilized AuNPs prepared by modular ultrasonic spray pyrolysis. J Nanomater. 2017;2017:1–17.

[21] Pareek V, Bhargava A, Gupta R, Jain N, Panwar J. Synthesis and applications of noble metal nanoparticles: a review. Adv Sci Eng Med. 2017;9(7):527–44.

[22] Rudolf R, Majerič P, Štager V, Albreht B. Process for the production of gold nanoparticles by modified ultrasonic spray pyrolysis: patent application no. P-202000079. Ljubljana: Office of the Republic of Slovenia for Intellectual Property. Slovenia, Ljubljana: Urad RS za Intelektualno Lastnino; 2020.

[23] Kucherik AO, Ryabchikov YV, Kutrovskaya SV, Al-Kattan A, Arakelyan SM, Itina TE, et al. Cavitation-free continuous-wave laser ablation from a solid target to synthesize low-size-dispersed gold nanoparticles. ChemPhysChem. 2017;18(9):1185–91.

[24] Tomko J, O'Malley SM, Trout C, Naddeo JJ, Jimenez R, Griepenburg JC, et al. Cavitation bubble dynamics and nanoparticle size distributions in laser ablation in liquids. Colloids Surf A Physicochem Eng Asp. 2017;522:368–72. doi: 10.1016/j.colsurfa.2017.03.030.

[25] John MG, Tibbetts KM. One-step femtosecond laser ablation synthesis of sub-3 nm gold nanoparticles stabilized by silica. Appl Surf Sci. 2019;475(January):1048–57. doi: 10.1016/j.apsusc.2019.01.042.

[26] Otto K, Oja Acik I, Krunks M, Tõnsuaadu K, Mere A. Thermal decomposition study of HAuCl4·3H2O and AgNO3 as precursors for plasmonic metal nanoparticles. J Therm Anal Calorim. 2014;118(2):1065–72.

[27] Abdelwahed W, Degobert G, Stainmesse S, Fessi H. Freeze-drying of nanoparticles: Formulation, process and storage considerations. Adv Drug Deliv Rev. 2006;58(15):1688–713.

[28] Beirowski J, Inghelbrecht S, Arien A, Gieseler H. Freeze-drying of nanosuspensions, 1: freezing rate versus formulation design as critical factors to preserve the original particle size distribution. J Pharm Sci. 2011;100(5):1958–68.

[29] Beirowski J, Inghelbrecht S, Arien A, Gieseler H. Freeze-drying of nanosuspensions, 2: the role of the critical formulation temperature on stability of drug nanosuspensions and its practical implication on process design. J Pharm Sci. 2011;100(10):4471–81.

[30] Beirowski J, Inghelbrecht S, Arien A, Gieseler H. Freeze-drying of nanosuspensions, part 3: investigation of factors

compromising storage stability of highly concentrated drug nanosuspensions. J Pharm Sci. 2012;101(1):354–62.

[31] De La Garza M, López I, Gómez I. *In situ* synthesis and deposition of gold nanoparticles with different morphologies on glass and ITO substrate by ultrasonic spray pyrolysis. Adv Mater Sci Eng. 2013;2013:1–5.

[32] Rahemi Ardekani S, Sabour Rouh Aghdam A, Nazari M, Bayat A, Yazdani E, Saievar-Iranizad E. A comprehensive review on ultrasonic spray pyrolysis technique: {Mechanism}, main parameters and applications in condensed matter. J Anal Appl Pyrolysis. 2019;141:104631.

[33] Jung DS, Park SBin, Kang YC. Design of particles by spray pyrolysis and recent progress in its application. Korean J Chem Eng. 2010 Nov;27(6):1621–45.

[34] Leng J, Wang Z, Wang J, Wu H-H, Yan G, Li X, et al. Advances in nanostructures fabricated *via* spray pyrolysis and their applications in energy storage and conversion. Chem Soc Rev. 2019;48(11):3015–72.

[35] Kim D, Kim Y, Hong S, Kim J, Heo N, Lee MK, et al. Development of lateral flow assay based on size-controlled gold nanoparticles for detection of hepatitis B surface antigen. Sens (Switz). 2016;16(12):2154.

[36] Fang C, Chen Z, Li L, Xia J. Barcode lateral flow immunochromatographic strip for prostate acid phosphatase determination. J Pharm Biomed Anal. 2011;56(5):1035–40. doi: 10.1016/j.jpba.2011.08.008.

[37] Amis TM, Renukuntla J, Bolla PK, Clark BA. Selection of cryoprotectant in lyophilization of progesterone-loaded stearic acid solid lipid nanoparticles. Pharmaceutics. 2020;12(9):1–15.

[38] Ravnik J, Ramšak M, Zadravec M, Kamenik B, Hriberšek M. Experimental and stochastic analysis of lyophilisation. Eur J Pharm Biopharm. 2021;159(November 2020):108–22.

[39] Innova Biosciences Guide. A guide to lateral flow immunoassays. 2020;44:1–15. Available from: https://fnkprddata.blob.core.windows.net/domestic/download/pdf/IBS_A_guide_to_lateral_flow_immunoassays.pdf.

[40] The Nativeantigen Company. Choosing the right reagents for your coronavirus immunoassay contents. Kidlington, Oxford: The NativeAntigen Company; 2020. p. 22. Available from: https://www.lubio.ch/assets/PDFs/Native_Antigen_Company_Choosing_The_Right_Reagents_for_Your_Coronavirus_Immunoassay.pdf.

[41] Rozand C. Paper-based analytical devices for point-of-care infectious disease testing. Eur J Clin Microbiol Infect Dis. 2014;33(2):147–56.

[42] Borse V, Srivastava R. Process parameter optimization for lateral flow immunosensing. Mater Sci Energy Technol. 2019;2(3):434–41.

[43] CrystalMaker Software Limited. CrystalMaker software. Begbroke: CrystalMaker Software Limited; 2021.

[44] Si J, Li J, Zhang L, Zhang W, Yao J, Li T, et al. A signal amplification system on a lateral flow immunoassay detecting for hepatitis e-antigen in human blood samples. J Med Virol. 2019;91(7):1301–6.

[45] Majerič P, Jenko D, Friedrich B, Rudolf R. Formation of bimetallic Fe/Au submicron particles with ultrasonic spray pyrolysis. Metals (Basel). 2018;8(4):1–13.

[46] Tiyyagura HR, Majerič P, Bračič M, Anžel I, Rudolf R. Gold inks for inkjet printing on photo paper: Complementary characterisation. Nanomaterials. 2021;11(3):1–13.

[47] Manta P, Nagraik R, Sharma A, Kumar A, Verma P, Paswan SK, et al. Optical density optimization of malaria pan rapid diagnostic test strips for improved test zone band intensity. Diagnostics. 2020;10(11):1–12.

[48] Byzova NA, Zherdev AV, Khlebtsov BN, Burov AM, Khlebtsov NG, Dzantiev BB. Advantages of highly spherical gold nanoparticles as labels for lateral flow immunoassay. Sens (Switz). 2020;20(12):1–15.

[49] Lan J, Ge J, Yu J, Shan S, Zhou H, Fan S, et al. Structure of the SARS-CoV-2 spike receptor-binding domain bound to the ACE2 receptor. Nature. 2020;581(7807):215–20. doi: 10.1038/s41586-020-2180-5.

[50] Huang Y, Yang C, Xu X, Xu W, Liu S. Structural and functional properties of SARS-CoV-2 spike protein: potential antivirus drug development for COVID-19. Acta Pharmacol Sin. 2020;41(9):1141–9. doi: 10.1038/s41401-020-0485-4.

[51] Al-Johani H, Abou-Hamad E, Jedidi A, Widdifield CM, Viger-Gravel J, Sangaru SS, et al. The structure and binding mode of citrate in the stabilization of gold nanoparticles. Nat Chem. 2017;9(9):890–5.